Pergamon

PII: S0301-9322(97)00025-6

Int. J. Multiphase Flow Vol. 23, No. 5, pp. 977–1001, 1997

Printed in Great Britain
0301-9322/97 $17.00 + 0.00

DEFORMABLE BUBBLES IN A FREE SHEAR LAYER

E. LOTH[1], M. TAEIBI-RAHNI[1] and G. TRYGGVASON[2]

[1]Department of Aeronautical and Astronautical Engineering, The University of Illinois, Urbana, IL 61801, U.S.A.

[2]Department of Mechanical Engineering and Applied Mechanics, The University of Michigan, Ann Arbor, MI 48109, U.S.A.

(Received 30 September 1996; in revised form 30 March 1997)

Abstract—The flow in and around three-dimensional deformable bubbles subjected to a non-linear planar free shear layer was simulated using a finite difference/front tracking scheme with the full Navier–Stokes equations including surface tension. This allowed detailed resolution of the flow around and inside the bubble. The bubble size and response time is comparable to the thickness and timescale of the free shear layer and we have investigated increased deformation by systematically lowering surface tension. The interaction between the bubble wake and the shear layer led to complex three-dimensional flows past and within the bubble surface. The resulting hydrodynamic forces and trajectories of the fully resolved bubble simulation could be qualitatively compared with those expected from quasi-steady classical predictions. In general, the quasi-steady drag began to underpredict the actual drag as deformation increased and the quasi-steady lift predicted values of opposite sign to that of the actual lift for very high deformation. © 1997 Elsevier Science Ltd.

Key Words: free shear layer, bubbles, deformable, drag, lift

1. INTRODUCTION

1.1. Previous studies

The convection and shape of deformable bubbles can be significantly affected by the local continuous phase turbulence. This is especially true if the temporal or spatial scale of the flow is of the order of that for the bubble. Such conditions can be described as having St or β of order unity, where St is the ratio of bubble response time to turbulent eddy lifetime and β is the ratio of bubble diameter to eddy size. Even for flows for which the global St or $\beta \ll 1$, we may find several small regions of strong gradients which yield a *local* St or β of order one (Oakley *et al.* 1995). Similarly, in a large eddy simulation of a bubbly flow, small bubbles may be of significant size and timescale with respect to the subgrid turbulence scales.

Understanding the hydrodynamic forces which act upon bubbles is critical to predicting bubble concentration distributions and turbulent dispersion processes. Most bubbly flow computations rely on a point bubble approximation and therefore a prescribed equation of motion. Such an approximation assumes the bubble mass is represented at a single point such that the resolution of the flow around the bubble surface is not necessary. With respect to point mass equations of motion for particles, Maxey and Riley (1983) derived a momentum equation for a small rigid sphere in an unsteady, non-uniform flow but limited to Stokesian flow conditions, i.e. particle Reynolds numbers of order one. Auton *et al.* (1988) derived a momentum equation for a body of simple shape moving through an inviscid fluid in which there is an unsteady, non-uniform, and rotational velocity field. Comparison of Auton's and Maxey–Riley's equations shows that the Faxen, Basset, and viscous effects have been neglected by Auton *et al.* (1988) and that the added mass term is slightly different due to Auton's inviscid flow assumption. In general, the equations derived from these two studies typify conventional point bubble equations of motion. Modifications of the force expressions used in such bubble dynamic equations to provide more fidelity have been the subject of much experimental and theoretical research (e.g. Kuo and Wallis 1988; Yang and Leal 1991; Jiang *et al.* 1993; Sangani and Didwania 1993; Lovalenti and Brady 1993).

In particular, the conventional bubble momentum equations which include Basset history and Faxen terms may become inadequate when St or β approaches unity for bubble Reynolds number (Re_B) much greater than one (Taeibi-Rahni *et al.* 1996). Additional complications arise when there is significant bubble deformation present. For example, experiments by Kojima *et al.* (1975) and Chahine *et al.* (1993) have shown that large deformable bubbles subjected to eddy fluctuations develop fundamentally different wakes as opposed to non-deformable ones. To fully describe such conditions, simulations must resolve the detailed fluid-bubble interaction.

Direct detailed description of the bubble internal and wake flow field have been presented by Chahine *et al.* (1993) and Chahine and Duraiswami (1992) for inviscid flows and Sangani and Didwania (1993) for non-deformable bubbles at large Reynolds numbers. However, simulations using the full three-dimensional Navier–Stokes equations while avoiding the point mass approximation are less common. Mei *et al.* (1991) used such a simulation for a solid particle in air and investigated the role of the Basset history effect. Unverdi and Tryggvason (1992a, 1992b) used such simulations but also included deformation to compute the collision of two bubbles using a front tracking technique. Ervin (1993) studied deformation of bubbles and drops in a linear shear using this technique and qualitatively verified the experimental results of Kariyasaki (1987), which suggests that deformable bubbles and droplets in linear shear flows can migrate in the opposite direction of solid particles, i.e. yield negative lift coefficients.

1.2. Present study

The objective of this study was to investigate the flowfields in and around high Re_B deformable bubbles in a non-linear free shear layer using direct numerical simulation to resolve all temporal and spatial scales. Herein, non-linear shear layer refers to one in which Kelvin–Helmholtz instabilities allow eddy and braid formation (as opposed to a linear shear layer of uniform velocity gradient throughout). The movement of the bubbles was based on the integral pressure and viscous forces over the surface of the bubble as defined by the local unsteady flow field, i.e. the empiricism of quasi-steady drag and lift coefficients was removed. Such a time-accurate Navier–Stokes formulation allows this study: (1) to directly observe the effect of the bubble interaction with eddies and braids for St and β of order unity; (2) to compare the actual hydrodynamic forces between the surrounding liquid and deformable bubbles with their conventional point bubble counterparts; and (3) to qualitatively assess the predictive ability of conventional bubble dynamic equations for bubble trajectories. In these respects, this study is unique.

2. NUMERICAL METHODS

2.1. RBS equations and numerical scheme

We avoid the point mass approximation herein by using a single-fluid model to compute the flow fields both inside and outside the bubble such that only one set of Navier–Stokes equations are used, instead of one for each phase separately. We shall refer to such a simulation as RBS (resolved bubble simulation) since all fluid dynamic scales are fully resolved spatially and temporally in and around the bubble itself. The RBS of this study employs a finite difference method combined with a front tracking scheme based on Unverdi and Tryggvason (1992a). The front tracking scheme uses an unstructured adaptive gird on the bubble surface in order to account for the bubble deformation. As such, the density and viscosity fields are advected by an explicit tracking of the contact discontinuity.

The numerical scheme used in this study computes the unsteady, incompressible, viscous, immiscible, multi-fluid, three-dimensional Navier–Stokes equations for the liquid and the gas. The evolution of both the free shear layer and the motion of the bubbles are governed by the same Navier–Stokes equation of momentum, which in conservative form, is

$$\frac{D(\rho \mathbf{V})}{Dt} = -\nabla p + \rho \mathbf{g} + \nabla\cdot(2\mu \mathbf{D}) + \sigma\kappa \mathbf{n}\delta(\mathbf{X} - \mathbf{X}^f), \qquad [1]$$

where $\mathbf{V}$ is the velocity vector, ρ is the density, μ is the viscosity, p is the hydrodynamic pressure, $\mathbf{D}$ is the rate of deformation tensor with components $D_{i,j} = (V_{i,j} + V_{j,i})/2$, σ is the surface tension coefficient, κ is twice the mean curvature, $\boldsymbol{g}$ is the gravity force, and $\mathbf{n}$ is an inward normal to the bubble surface. Surface tension has been added as a delta function, $\delta(\mathbf{X} - \mathbf{X}^{\mathrm{f}})$, which is non-zero only on the bubble surface, where $\mathbf{X} = \mathbf{X}^{\mathrm{f}}$. This equation is complemented by the incompressibility condition

$$\nabla \cdot \mathbf{V} = 0 \qquad [2]$$

which leads to an elliptic pressure equation when combined with the Navier–Stokes equations.

The density and viscosity are allowed to vary, such that the above equations are therefore valid for the whole flow field (both the bubble and the ambient liquid flow fields). The resulting two continuity equations simply state that the density and viscosity of a fluid particle does not change

$$\frac{\partial \rho}{\partial t} + \mathbf{V} \cdot \nabla \rho = 0, \quad \frac{\partial \mu}{\partial t} + \mathbf{V} \cdot \nabla \mu = 0. \qquad [3]$$

In order to capture the discontinuity of the flow between the gas and the liquid, an indicator *function*, $I(\mathbf{X})$ is constructed using the known position of the points on the bubble surface. This function is 0 for the outer liquid and 1 for the gas inside the bubble such that the density and viscosity fields can be written in terms of $I(\mathbf{X})$ as follows

$$\rho(\mathbf{X}) = \rho_{\mathrm{L}} + (\rho_{\mathrm{B}} - \rho_{\mathrm{L}})I(\mathbf{X}), \quad \mu(\mathbf{X}) = \mu_{\mathrm{L}} + (\mu_{\mathrm{B}} - \mu_{\mathrm{L}})I(\mathbf{X}), \qquad [4]$$

where subscript B signifies bubble properties and subscript L signifies the liquid outside the bubble.

The tracking of a bubble front within the computational domain is achieved by incorporating a (bubble) surface grid within a volumetric grid. Therefore, discretization of the field equations is carried out on two sets of embedded meshes: (a) the Eulerian *fluid grid*, which is three-dimensional, cubical, staggered, structured, and non-adaptive; and (b) the Lagrangian *front grid*, which is two-dimensional, triangular, unstructured, and adaptive.

The Navier–Stokes equations are solved by a relatively standard finite difference projection method on the staggered three-dimensional Eulerian fluid grid. All spatial derivatives are evaluated by second order centered differences, and the time integration is performed by a second order predictor–corrector method. The pressure equation, which is non-separable since the density is not constant, is solved by a Black and Red SOR iteration technique.

To advect the discontinuous density and viscosity fields, and to compute surface tension forces, we represent the bubble surface by the front grid computational elements. The two-dimensional front grid is advected by the fluid velocity which is interpolated from the three-dimensional fluid grid. To inject surface tension forces onto the fixed fluid grid we use a technique that is usually called the immersed boundary method and was introduced by Peskin (1977) for simulations of the motion of the heart. In this approach, the infinitely thin boundary is approximated by a smooth distribution function that is used to distribute the surface forces over the grid points close to the surface in such a way that the total forces are conserved. Therefore, the front is given a finite thickness of about three to four grid spacings and there is no numerical diffusion of this front since this thickness remains constant for all time. To generate the density and viscosity fields from the front we use a technique which is based on distributing the jump in these quantities onto the fixed grid by Peskin's scheme and then solving a Poisson equation for the field variable itself. This technique is presented in more detail by Unverdi and Tryggvason (1992a).

2.2. Computation of hydrodynamic forces based on RBS results

From the RBS flow field, we can solve for the instantaneous bubble hydrodynamic forces of drag and lift by applying a bubble momentum equation *a posteriori* to the predicted bubble and liquid flowfields. To do so requires calculation of several liquid flow characteristics at the bubble location. For large resolved bubbles, it is not possible to define one particular point in the liquid flow field which fully represents the local surrounding liquid properties (as is normally done in two-fluid models which assume a point bubble). Therefore, the local liquid quantities, such as liquid velocity

around the bubble, $\mathbf{V}_L$, are herein approximated by spatially integrating the computed vector field in a region close to the bubble (similar to Soo 1976). For the finite bubble Reynolds numbers of this study, e.g. 40, we assume the bubble is influenced in an approximately inviscid manner by the surrounding flow, i.e. with a $1/r^3$ dependence. This dependence was coupled with a volume integration within the region of one to three diameters away from the bubble centroid (defined as Vol_L). The inner limit avoids the bubble boundary layer and excludes the virtual mass of the fluid which normally moves with the bubble. Thus, the averaged value of a liquid characteristic, say Q, for which the bubble was considered immersed, was taken as

$$Q_{ave} = \int_{Vol_L} \frac{Q(r)}{r^3}\, d(Vol) \Big/ \int_{Vol_L} \frac{1}{r^3}\, d(Vol). \quad [5]$$

As such, the instantaneous bubble velocity relative to the average flow velocity in the vicinity of the bubble, $\mathbf{V}_{rel}$, is taken to be $\mathbf{V}_B - \mathbf{V}_{L,ave}$, where $\mathbf{V}_B$ is based on the trajectory of the bubble volumetric centroid and $\mathbf{V}_{L,ave}$ is computed using [5]. This spatial integration was evaluated with rising bubble studies where the resulting relative velocities were accurate to within 2% (Taeibi-Rahni 1995). Changing the upper bound of the spatial integration from 3 to 4 diameters yielded differences of only 3% for both rising bubbles and shear layer bubbles.

Once the above time varying flow field and history of the bubble characteristics were obtained, we applied the following methodology *a posteriori* on the RBS results to determine the drag and lift forces. Since these forces include effects of non-linear spatial and temporal flow gradients as well as deformation, we will refer to them as *total* lift and drag forces ($\mathbf{D}'_{tot}$, $\mathbf{L}'_{tot}$). The bubble dynamic equation of Auton *et al.* (1988), is herein generalized to include these total forces as follows

$$(\rho_B + \rho_L C_m) Vol_B \frac{d\mathbf{V}_B}{dt} = Vol_B(\rho_B - \rho_L)\mathbf{g} + \mathbf{D}'_{tot} + \mathbf{L}'_{tot} + Vol_B \left\{ \rho_L \left[(1 + C_m) \frac{D\mathbf{V}_{L,ave}}{D_t} \right] \right\}, \quad [6]$$

where

$$\frac{d(\ )}{dt} = \frac{\partial(\ )}{\partial t} + \mathbf{V}_B \cdot \nabla(\ ) \quad [7]$$

and

$$\frac{D(\ )}{Dt} = \frac{\partial(\ )}{\partial t} + \mathbf{V}_{L,ave} \nabla(\ ) = \frac{d(\ )}{dt} - (\mathbf{V}_B - \mathbf{V}_{L,ave}) \cdot \nabla(\ ). \quad [8]$$

Note $(\ )'$ here signifies forces before normalization by $[2\rho_L(\Delta u)^2 Vol_B/(\pi d_B)]$ for which d_B is the original bubble diameter and Vol_B is the bubble volume based on d_B. In the above equation, C_m is the added mass coefficient ($=1/2$, Auton *et al.* 1988). Note, C_m can vary with acceleration number, which is the ratio of convective acceleration to local bubble acceleration (Odar and Hamilton 1964). However, using Odar's expression for the added mass coefficient yielded small

Table 1. List of cases with bubble surface tensions

Cases	Bubble placement	σ	Morton number	Bond number
A3 (rising bubble)	Quiescent flow	40	4.5×10^{-11}	0.033
C3 (single phase)	None	None	—	—
G3 (shear layer)	Left vortex core	40	4.5×10^{-11}	0.033
G3d (shear layer)	Left vortex core	4	4.5×10^{-8}	0.33
G3dd (shear layer)	Left vortex core	1	2.9×10^{-6}	1.3
G3ddd (shear layer)	Left vortex core	0.5	2.3×10^{-5}	2.6

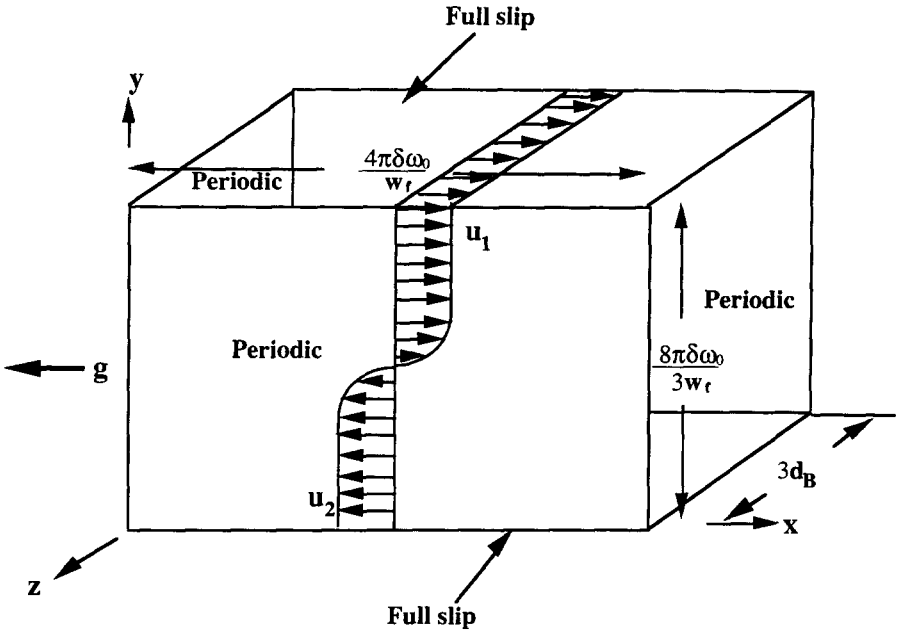

Figure 1. Computational domain with boundary and initial conditions, where there are periodic boundary conditions at x–y and y–z walls and full slip boundary conditions at x–z walls.

differences (3%) as compared Auton's with respect to the computed drag and lift forces (Taeibi-Rahni 1995). Therefore, Auton's value of 1/2 was used for the results presented herein.

In [6], the forces in the right hand side are buoyancy ($\mathbf{B}'$), total drag and lift ($\mathbf{D}'_{tot}$ and $\mathbf{L}'_{tot}$), and the force resulting from the stress gradients of the liquid flow in the absence of a bubble ($\mathbf{S}'$). All these forces equate to the bubble mass and the added mass times the bubble acceleration on the left-hand side ($\mathbf{I}'$). As noted by Maxey and Riley (1983), the stress gradient term includes both pressure and viscous stress gradients acting on the bubble. Thus, the total lift and drag forces were computed by decomposing [6] into the drag and lift directions

$$\mathbf{D}'_{tot} = \mathbf{I}'_D - \mathbf{B}'_D - \mathbf{S}'_D \qquad [9]$$

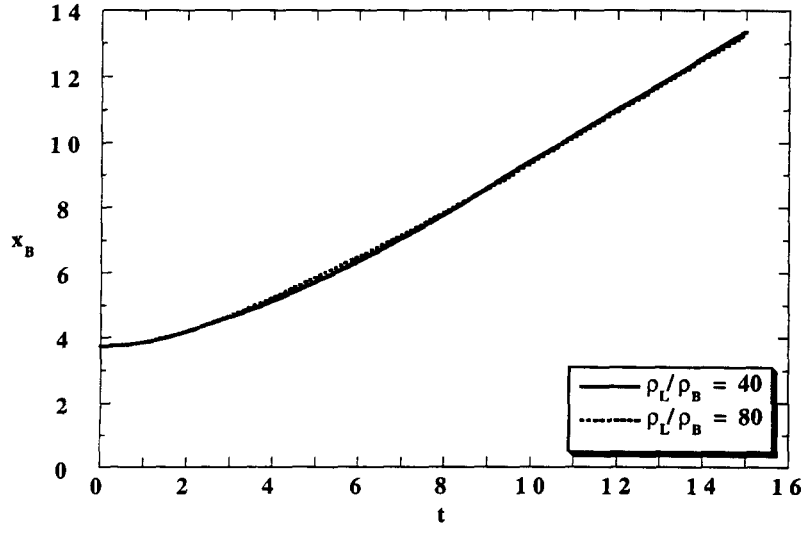

Figure 2. Comparison of time history of the bubble displacement with two different density ratios for case A3.

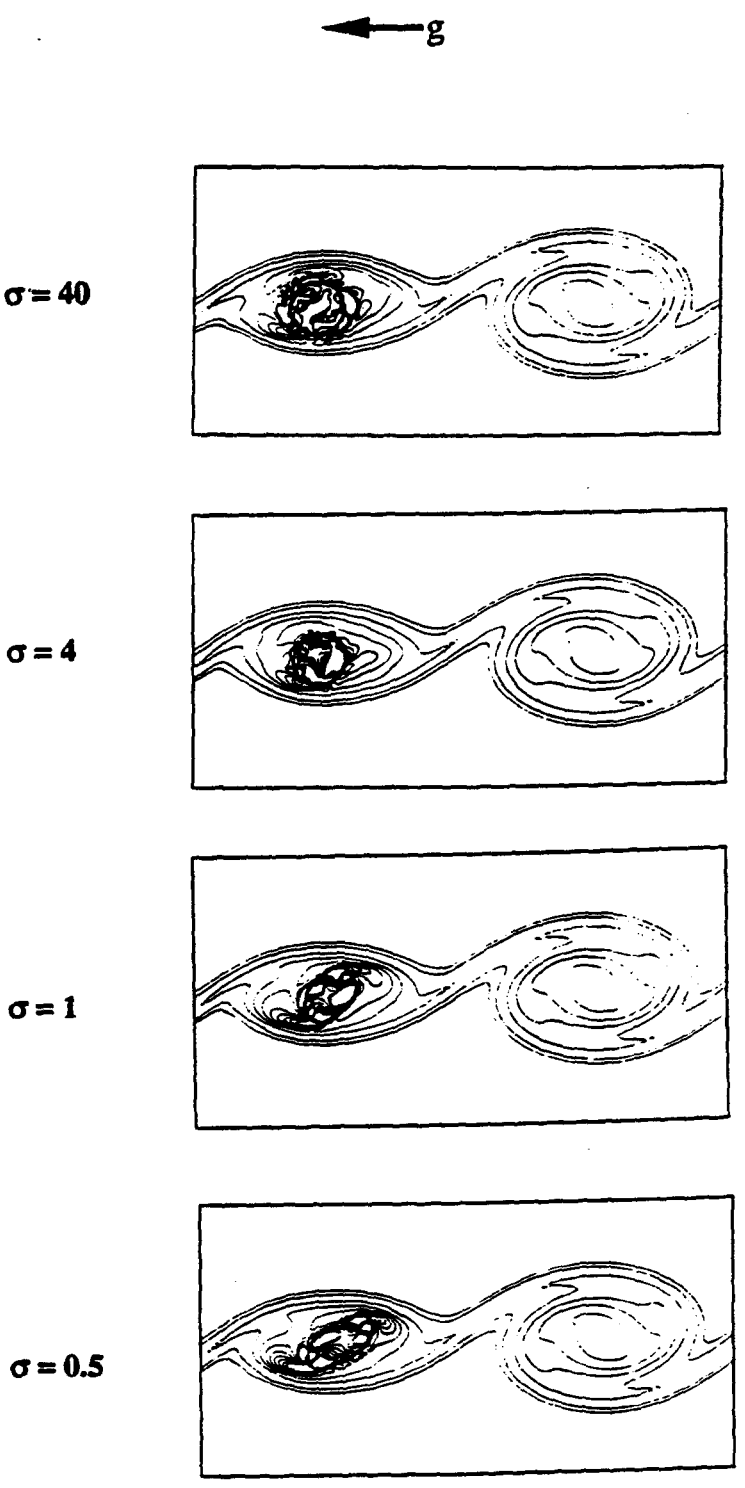

Figure 3. ζ_z at $t = 10$ for cases G3 ($\sigma = 40$), G3d ($\sigma = 4$), G3dd ($\sigma = 1$), and G3ddd ($\sigma = 0.5$).

and

$$\mathbf{L}'_{tot} = \mathbf{I}'_L - \mathbf{B}'_L - \mathbf{S}'_L. \quad [10]$$

Several numerical sensitivity studies were completed to determine the components which contribute to the overall 25% uncertainty of the forces and 10% uncertainty of $\mathbf{V}_{rel}$. Individual uncertainties included differences attributed to formulation of C_m ($\sim 3\%$) for the spherical case, spatial and

temporal resolution of $\mathbf{V}_L$ ($\sim 2\%$), spatial averaging errors ($\sim 9\%$), and errors in relative velocity angle ($\sim 3\%$); for details see Taeibi-Rahni (1995).

For later comparison with the above total lift and drag expressions we can also compute the conventional quasi-steady counterparts. The quasi-steady drag on a bubble can be written as

$$\mathbf{D}'_{QS} = -k_D C_{DQS} \rho_L (\pi d_B^2/8) |\mathbf{V}_{rel}| \mathbf{V}_{rel}, \qquad [11]$$

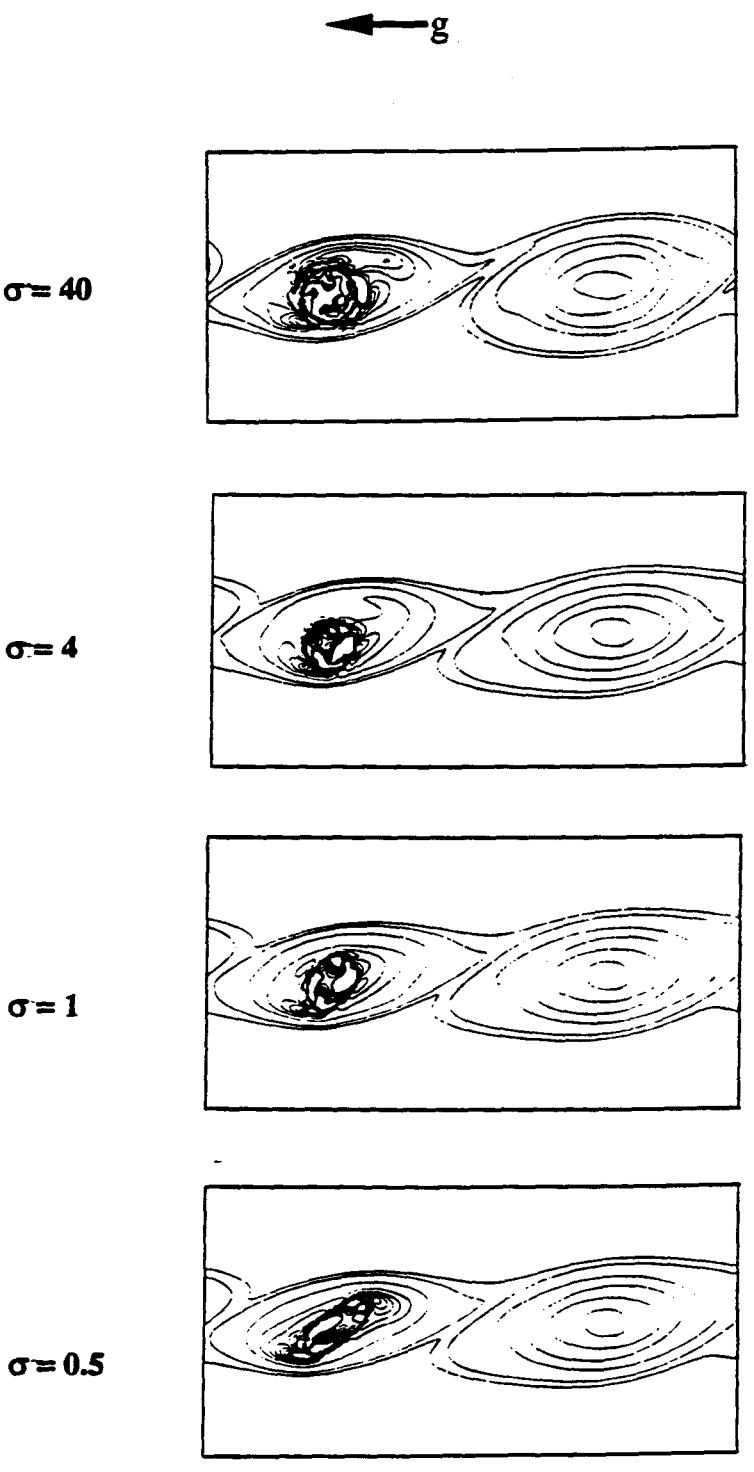

Figure 4. ζ_z at $t = 15$ for cases G3 ($\sigma = 40$), G3d ($\sigma = 4$), G3dd ($\sigma = 1$), and G3ddd ($\sigma = 0.5$).

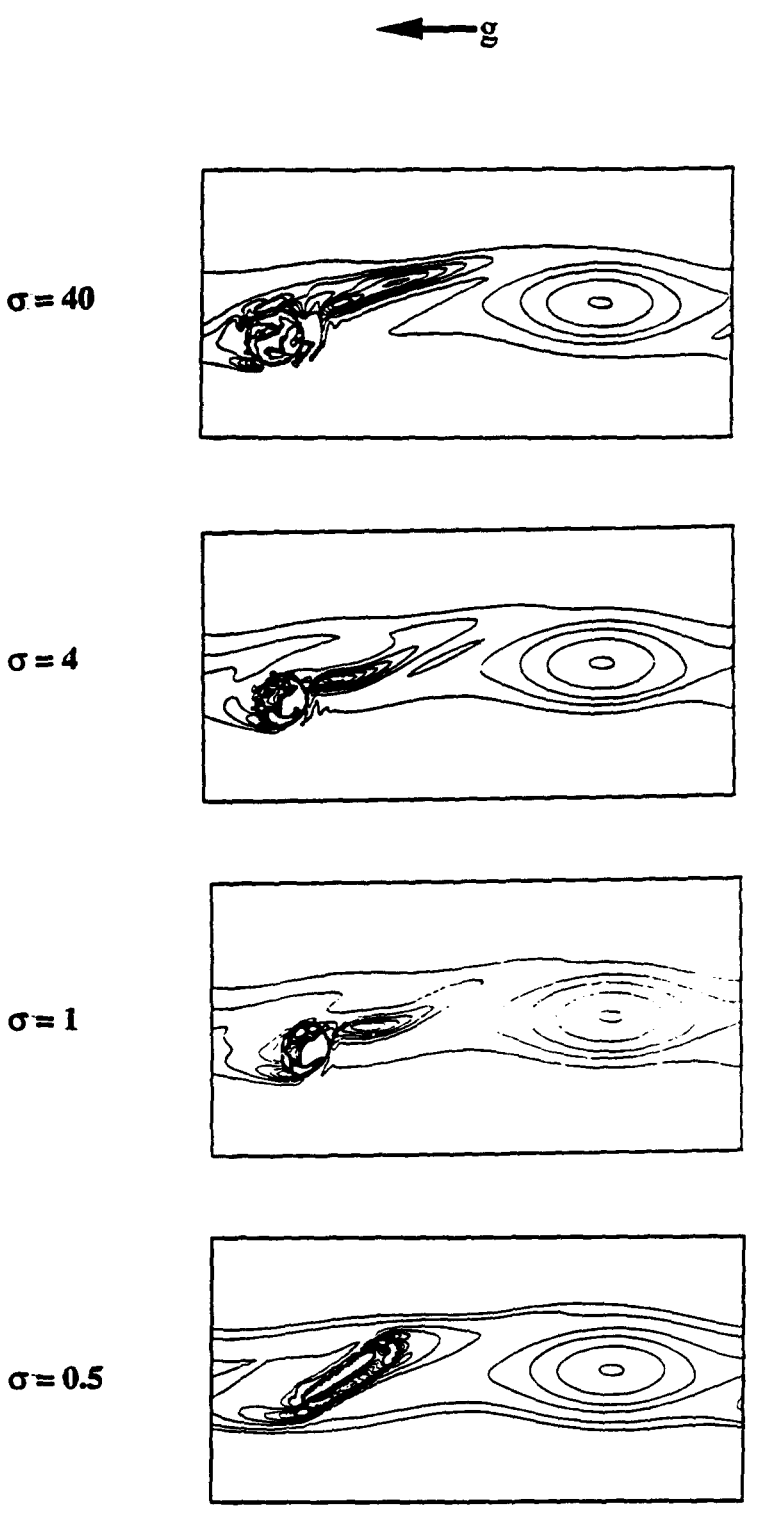

Figure 5. ζ_z at $t = 20$ for cases G3 ($\sigma = 40$), G3d ($\sigma = 4$), G3dd ($\sigma = 1$), and G3ddd ($\sigma = 0.5$).

where C_{DQS} is the quasi-steady drag coefficient for a solid sphere. This value was taken from White (1991) as

$$C_{DQS} = \frac{24}{Re_B} + \frac{6}{1 + \sqrt{Re_B}} + 0.4,$$

(a)

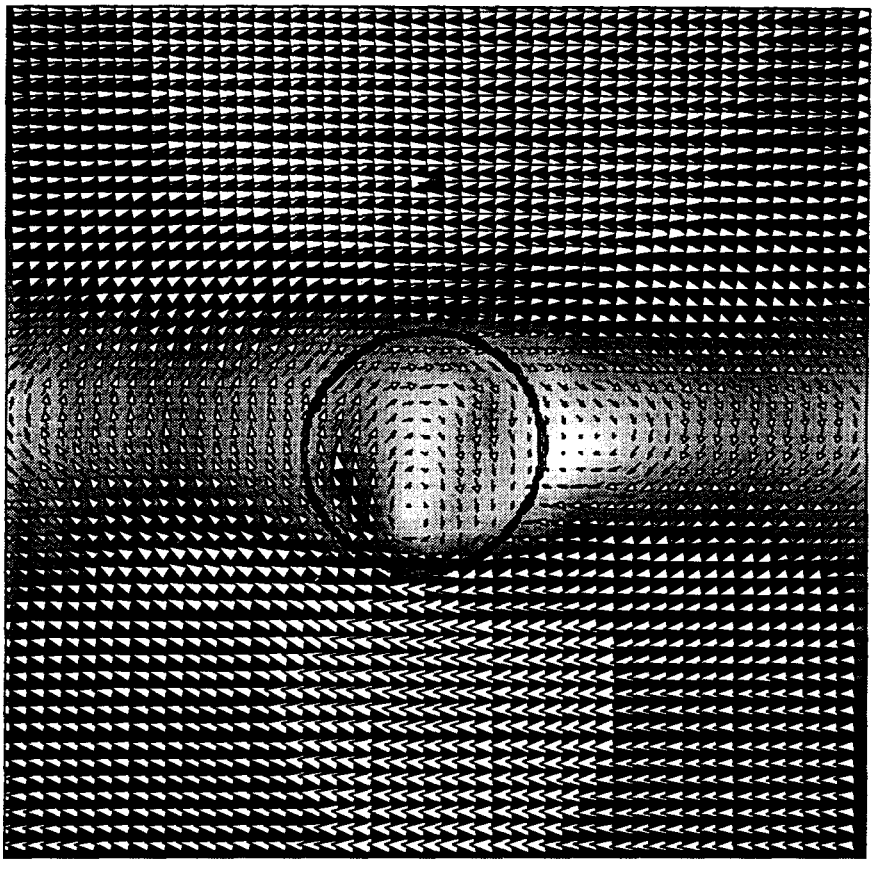

(b)

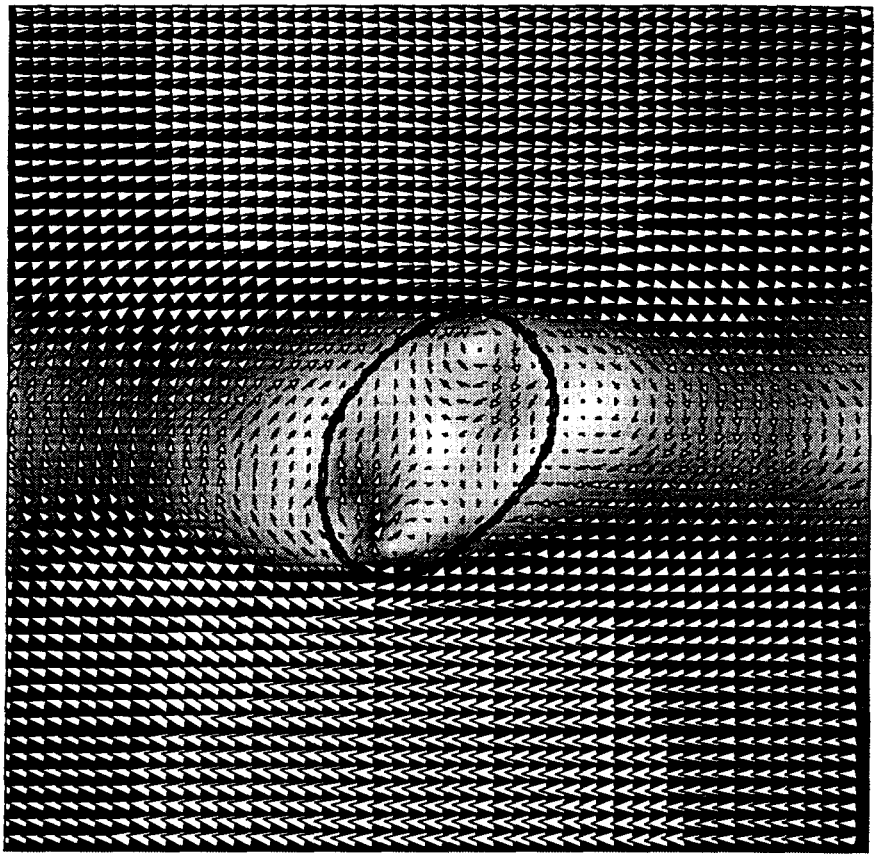

Fig. 6. (a), (b)—(*caption overleaf*)

(c)

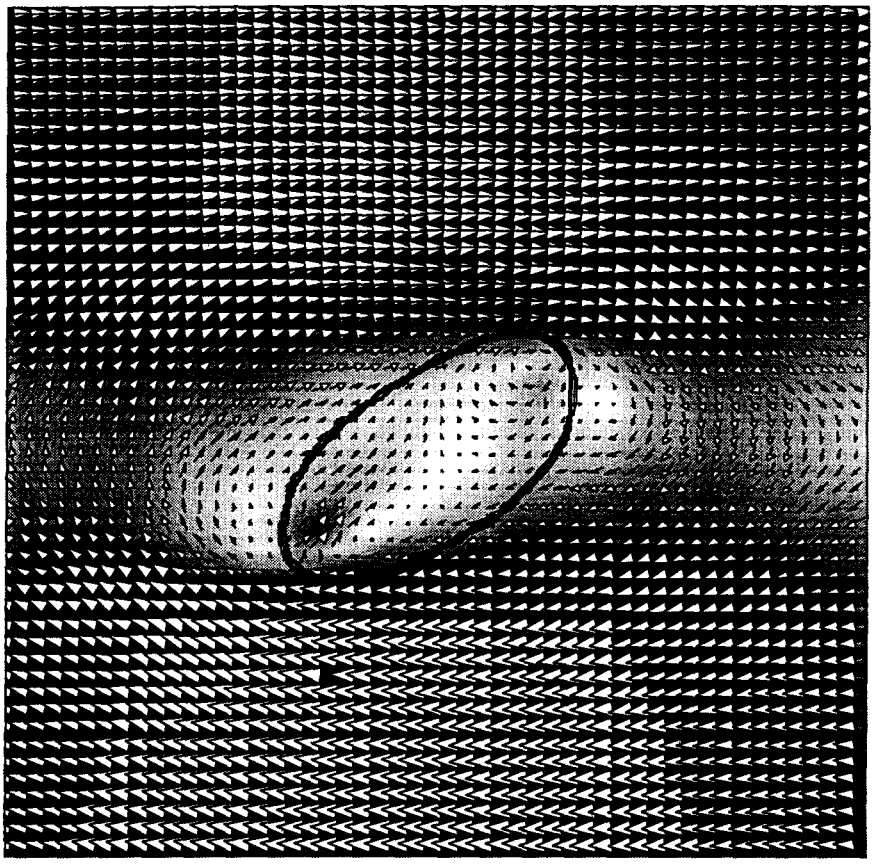

Figure 6. Close-up of relative velocity vectors in the x–y plane with q_{rel} in the background at $Re_B \sim 11$ corresponding to $t = 10$ for (a) case G3d ($\sigma = 4$), (b) case G3dd ($\sigma = 1$), (c) case G3ddd ($\sigma = 0.5$).

where k_D is the ratio of drag coefficient of a fluid body to that of a solid body taken from Sherman (1990) as 4.03/6, and $\mathbf{V}_{rel}$ is the relative velocity of the bubble with respect to the fluid ($\mathbf{V}_B - \mathbf{V}_{L,ave}$). A different formulation of the quasi-steady drag (C_{DQS}) which is proposed for a bubble at finite Reynolds numbers in unsteady fluid based on Mei (1994) was also examined.

For the quasi-steady lift, the following inviscid formulation is used

$$\mathbf{L}'_{QS} = -C_{LQS}\rho_L(4\pi d_B^3/24)(\mathbf{V}_{rel} \times \omega)_{ave}, \quad [12]$$

where C_{LQS} is the quasi-steady lift coefficient ($=1/2$, Auton *et al.* 1988) and ω is the vorticity of the liquid around the bubble. A second quasi-steady lift formulation using a viscous Saffman (1956) formulation will also be considered for comparison with the total lift. Although such a lift force is conventionally used for only very low bubble Reynolds numbers, it is considered herein since it was shown by Sridhar and Katz (1993) that for small *spherical* bubbles with Re_B of order 10^2, $\omega^{1/2}$ was a better scaling for lift than ω. Therefore, we will consider a second quasi-steady *viscous* lift as follows

$$L'_{vQS} = C_{LvQS}\rho_L \mathbf{V}_{rel}(d_B^2/4)(v\omega)^{1/2}, \quad [13]$$

Saffman derived a C_{Lv} of 6.46 for $Re_B < 1$, while Sridhar and Katz (1993) empirically found a value of 12.8 for bubble Reynolds numbers of 20–80. Since the latter is more typical of the present conditions, we shall use $C_{LvQS} = 12.8$.

The differences between total drag and lift forces based on the RBS and based on the quasi-steady counterpart values arise due to the aspects of bubble deformation as well as the strong unsteadiness and non-uniformity of the surrounding flow, e.g. the Basset history and the Faxen effects. We might expect the most dramatic differences to occur at values of St and β of order unity (and $Re_B \gg 1$), as is the case herein.

2.3. *Point bubble trajectories*

A separate set of computations (beyond the RBS) were completed using a point bubble approximation to compute trajectories using the modified Auton *et al.* (1988) bubble dynamics equation introduced earlier [6]. However, instead of solving for total drag and lift, the quasi-steady drag and lift forces described above (which can be readily calculated) were used in their place to solve for instantaneous bubble acceleration (and thus velocity and trajectory).

The liquid properties (such as $\mathbf{V}_L$, $\nabla\mathbf{V}_L$, and ω) for the point bubble were spatially interpolated from the time-developing flow field of case C3 (single-phase) for each time increment. Thus we are assuming that the bubble induced motions do not significantly alter the shear layer. While local flow variations were observed, global turbulent statistics indicated that such an assumption was reasonable, e.g. time history of the spatially averaged shear layer thickness and vertical Reynolds stress distribution for all bubbly shear layer simulations exhibited negligible differences, e.g. less than 2% (Taeibi-Rahni 1995). This is consistent for the low void fractions we are employing herein ($\sim 1\%$) as per Loth and Cebrzynski (1995). Note, no spatial averaging of liquid properties (i.e. [5]) was necessary for these point bubble calculations.

The objective of the point bubble trajectory study is to understand the differences between the way a point bubble and a large bubble (simulated with RBS) convect in a two-phase mixing layer. Recall, the point bubble is typically assumed to encounter flows which are of lower frequency than that of the bubble itself and significantly larger length scale than of the bubble diameter.

2.4. *Boundary and test conditions*

Computationally, there are two different approaches to studying the development of a non-linear free shear layer between two parallel streams with different velocities: spatially evolving and temporally evolving. A temporally evolving shear layer does not contain the subtleties of asymmetric entrainment mechanisms, but the vorticity field is essentially invariant with regard to changes of inertial frame. The approach herein is to use a temporally evolving shear layer as it saves an order of magnitude on computational requirements. The temporal free shear layer development employed periodic boundary conditions for the left and right boundaries and front and back boundaries, as well as full slip conditions for the top and bottom walls. A fundamental perturbation and a 90° out-of-phase sub-harmonic superimposed on a hyperbolic tangent mean profile was employed based on the results of Metcalfe *et al.* (1987) to yield the fastest vortex pairing. The dimensional initial velocity used in this study had the form

$$u(x, y, 0) = u_1 \tanh(y/\delta_{\omega 0}) + 2u_1 \operatorname{sech}(y/\delta_{\omega 0})\{e_f \cos[w_f(x + \theta)] + e_S \cos(w_S x)\}, \qquad [14]$$

where $u_1 = 2$, $e_f = 0.2$, $e_S = 0.14$, $w_f = 0.4446$, $w_S = w_f/2$, and $\theta = \pi/2w_f$. All length scales were thus normalized by the initial vorticity thickness ($\delta_{\omega 0} \equiv u_1/(\mathrm{d}u/\mathrm{d}y)_{max}$), the velocity scales by $u_1/2$, and the time scales by the ratio of these two values. In order to yield two full fundamental waves, a flow domain of width $4\pi/\omega_f$ and height of $8\pi/3\omega_f$ is used (see figure 1). Note the domain thickness was set at $3d_B$ which was shown by Taeibi-Rahni (1995) to be sufficiently wide such that the influence of the image bubbles moving in *parallel* to each other was not strong. A shear layer Reynolds number ($\mathrm{Re}_{\delta 0} \equiv \rho_L \Delta u \delta_0/\mu_L$) of 250 was chosen, where δ_0 is based on a 5–95%Δu velocity profile thickness for which the velocity difference (Δu) is defined as $u_1 - u_2$. At such a $\mathrm{Re}_{\delta 0}$, the liquid flow is unsteady and non-linear but too viscous to begin a transition to turbulent flow.

The kinematic viscosity ratio, ν_L/ν_B, was set as 0.085, close to that of water to air. The density ratio was investigated to note its influence on bubble movement. The effect of increasing the density ratio effect on the streamwise movement and velocity of case A3 (rising bubble) was found to be small. This is demonstrated in the plot of streamwise movement as a function of time (figure 2) for ρ_L/ρ_B of 40 and 80 (where ρ_L was fixed as 1 for both cases). Therefore, a ρ_L/ρ_B of 40 was used for the cases reported herein since higher ratios did not lead to significant changes in the flow but significantly increased computational time.

For the shear layer simulations, the bubbles were added near the left vortex core to the single-phase free shear layer flow at $t = 5$ after the initial shear layer conditions. By this time, two large eddies and a middle braid had developed due to Kelvin–Helmholtz instability. The internal

(a)

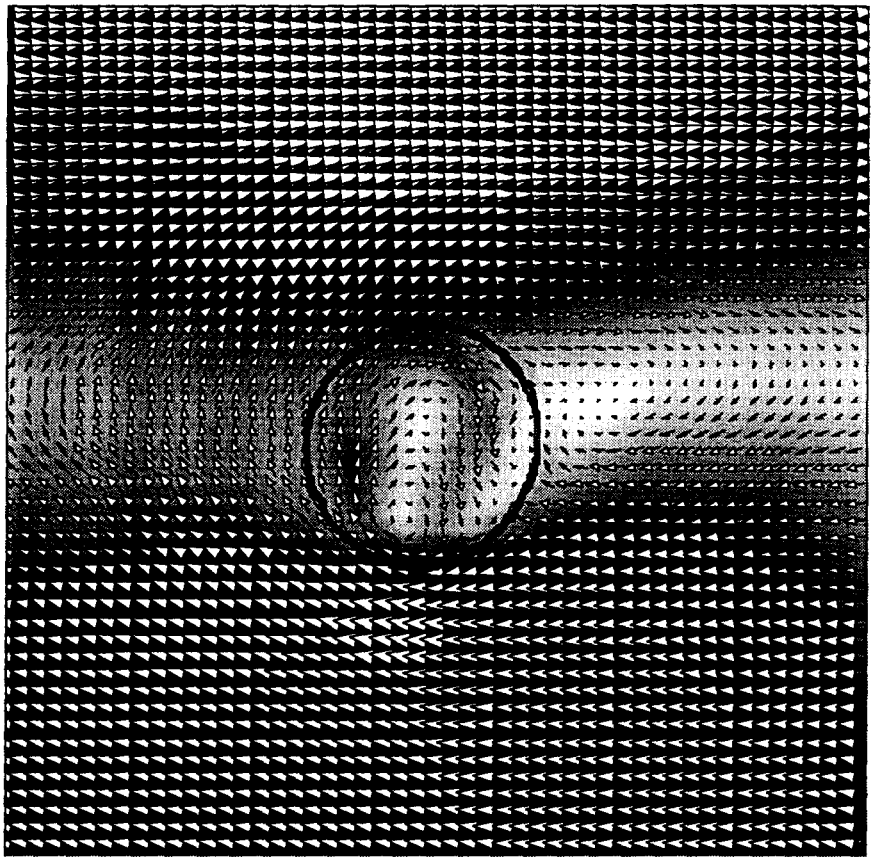

(b)

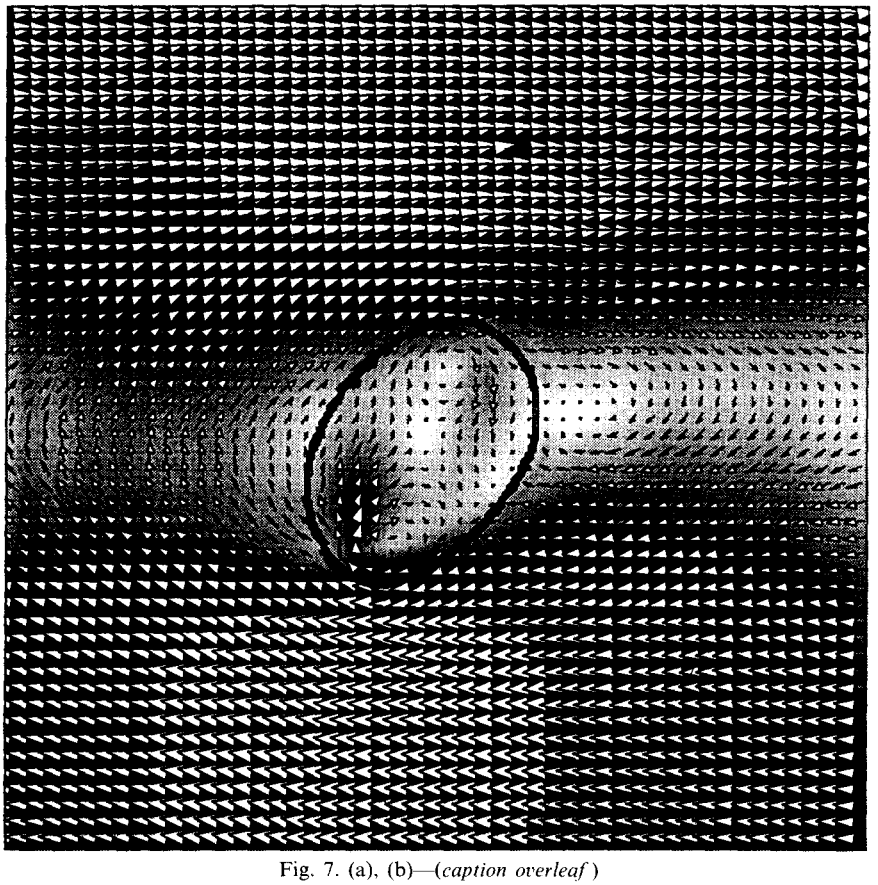

Fig. 7. (a), (b)—(*caption overleaf*)

(c)

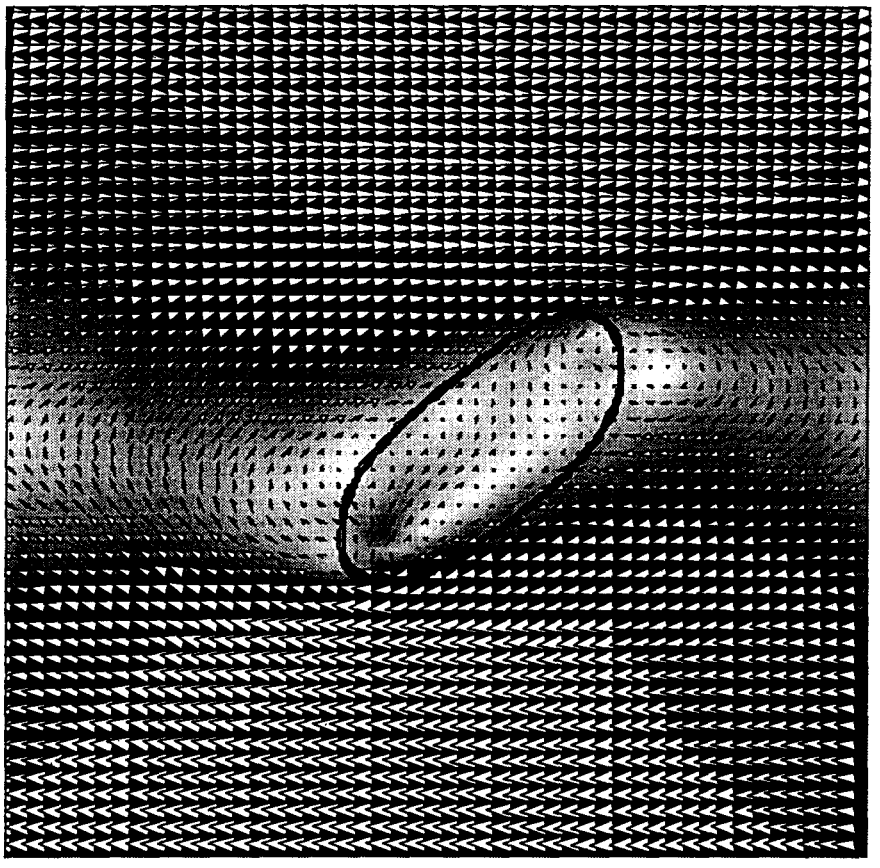

Figure 7. Close-up of relative velocity vectors in the x–y plane with q_{rel} in the background at $Re_B \sim 11$ corresponding to $t = 15$ for (a) case G3d ($\sigma = 4$), (b) case G3dd ($\sigma = 1$), (c) case G3ddd ($\sigma = 0.5$).

bubble velocities were simply initialized to equal that of the liquid velocities that were being replaced, i.e. they were unchanged. The initial bubble shape (which was always spherical) was then used to compute the indicator function and therefore the new density and viscosity distributions using [4]. In this study, the magnitude of the gravity ($\boldsymbol{g} = 0.206$), the velocity difference ($\Delta u = 4$) and the initial shear layer thickness ($\delta_0 = 3.8$) were chosen such that centrifuge forces would be stronger than buoyancy forces based on the value of the eddy Froude number ($F_{r\delta 0} \equiv \Delta u^2/4g\delta_0 = 5$). Thus, the bubbles are expected to stay near the vortex core rather than move uniformly in the $-\boldsymbol{g}$ direction. In addition, the bubble diameter ($d_B = 2.5$) was chosen such that bubble response time was of the same order as the shear layer timescale (St ~ 0.6, based on terminal velocity of bubble in case A3), and bubble size was of the same order as the shear layer thickness ($\beta \sim 0.7$, based on δ_0). Thus, the bubbles are expected to 'see' spatial and temporal gradients which can lead to significant departure from quasi-steady conditions, i.e. St and β of order unity.

The Bond number (also called the Eotvos number) and the Morton number have the main role in how a bubble is deformed in the absence of significant liquid flow gradients (Clift *et al.* 1978). The Bond number ($B \equiv \rho_L g d_B^2/\sigma$) is based on the interfacial surface tension (σ) and is the ratio of internal hydrodynamic pressure force to the surface tension force. The Morton number ($M \equiv g\mu_L^4/\rho_L\sigma^3$) is a property group which contains the additional influence of viscosity. The case designation and surface tension parameters are listed in table 1. These values of surface tension were chosen to give a wide range of bubble deformation: from nearly spherical to ellipsoidal to oblate.

In order to find an appropriate mesh size (Δx), several resolution studies were performed with and without bubbles in the shear layer. Taeibi-Rahni *et al.* (1995) showed that a cell Reynolds number ($Re_{cell} \equiv \rho_L \Delta u \Delta x/\mu_L$) of about 24 was needed for an accurate grid independent solution with a $Re_{\delta 0}$ of 250. This was demonstrated by examining vorticity variance, since vorticity is a very

sensitive indicator of grid resolution. The average variance between the vorticity fields from $Re_{cell} = 24$ to 19 was about 1% of the maximum vorticity. Therefore, a Re_{cell} of 24 was used along with an Eulerian fluid grid of $144 \times 96 \times 38$ for all the single-phase and bubbly free shear layer simulations (cases C3, G3, G3d, G3dd, G3ddd). A typical shear layer simulation with a bubble required about 550,000 points, 30 CPU hours and 16 MW on a Cray C90. A rising bubble simulation was also completed with a quiescent surrounding liquid (case A3) with a grid of $144 \times 38 \times 38$.

(a)

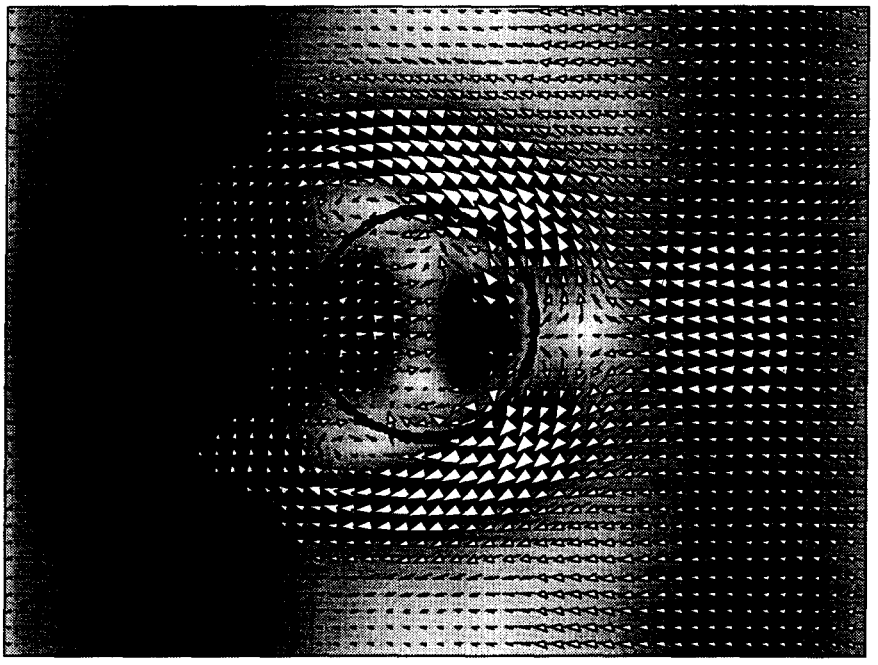

(b)

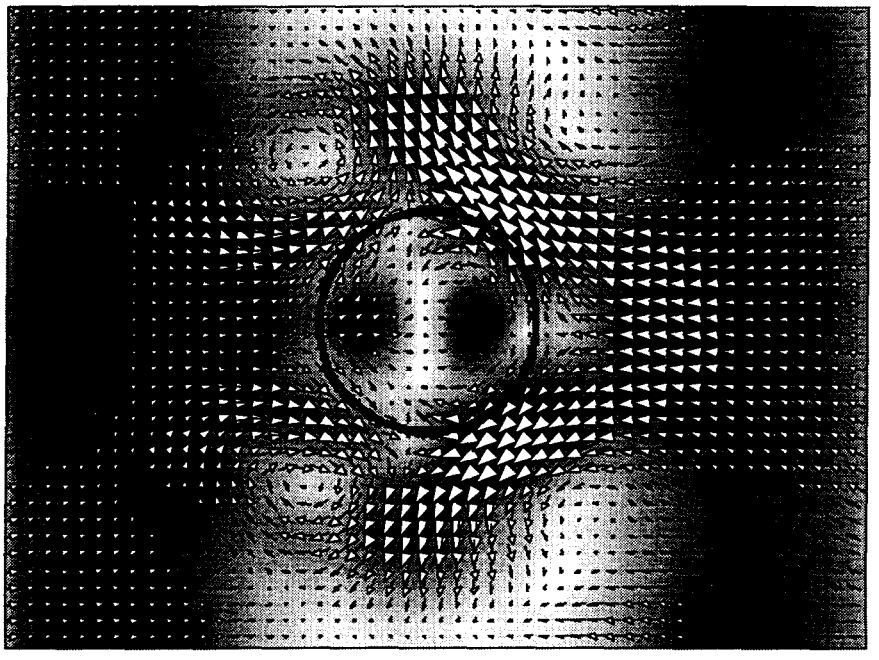

Fig. 8. (a), (b)—*(caption facing page)*

(c)

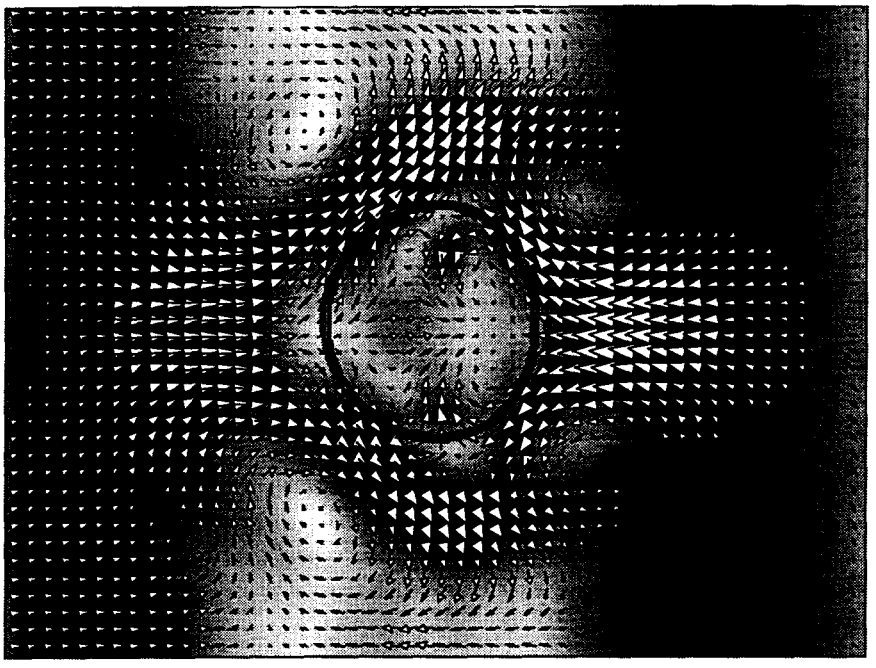

Figure 8. Close-up of relative velocity vectors in the x–z plane with q_{rel} in the background at $Re_B \sim 11$ corresponding to $t = 15$ for: (a) case G3d ($\sigma = 4$), (b) case G3dd ($\sigma = 1$) (c) case G3ddd ($\sigma = 0.5$).

3. RESULTS AND DISCUSSION

3.1. *Liquid vorticity evolution*

Contours of spanwise Favre-average (density-weighted) vorticity ($\zeta_z \equiv \rho\omega_z$), which serve as markers of the vortex structures and strength, were used in figures 3–5 for visualization of the liquid flow field interacting with the large bubbles. The contour increments are all the same: 10% of the difference between maximum and minimum vorticity noted in the single-phase computation. All these figures are slices of the flow field through the centroid of the bubble in the x–y plane (note, the bubble stays very close to the center of the domain in the z-direction). Dark gray contours of the front are also superimposed on the vorticity contours to reveal the finite thickness associated with the variation of density and viscosity normal to the bubble surface.

Figure 3 shows the contours of ζ_z for cases G3, G3d, G3dd, G3ddd at $t = 10$. At this time, two eddies have fully developed and the bubble is still trapped in the left eddy for all cases. Gravity has pulled the bubbles slightly to the right of the eddy core. The bubble deformation is consistent with convection of the upper and lower parts of the bubble in the clockwise direction to the surrounding eddy being somewhat elongated in the horizontal direction. The increasing deformity of cases G3d, G3dd and G3ddd corresponds to the systematic reduction in surface tension. Note, case G3 yields sharper flow gradients at its surface as compared to the other cases which have a more relaxed deformation. This is due to the additional resistance of the bubble surface to the internal and external flows at high surface tension.

At $t = 15$ (figure 4), the same effects are present, but are somewhat more pronounced. As the eddy core descends and moves to the left, the bubbles tend to follow, although less so for the more deformable cases. The pairing process has started and thus local eddy stretching is apparent (slightly less advanced locally for case G3). The deformation of the bubble of case G3dd is about the same as before, while that of case G3ddd has increased considerably. This is perhaps due to the increased proximity to the vortex core for the G3dd bubble.

Figure 5 shows the ζ_z contours at $t = 20$ for cases G3, G3d, G3dd, and G3ddd. Between $t = 15$ and 20, the bubble motion with respect to the eddy has changed significantly for the first three cases as they have 'overshot' the eddy core; this is due to the greater acceleration exhibited on a buoyant particle as compared to a neutrally buoyant liquid particle in a liquid acceleration. The subsequent movement of the bubble to the left as it goes below the eddy core indicates convection

dominates the buoyancy force (which is to the right). The deformation direction is again consistent with that noted at $t = 15$. Also as the surface tension has decreased, the wake of the bubble appears progressively reduced and in case G3ddd, the flow around the bubble is almost fully attached. However, velocity vector plots (in the next section) will show that significant three-dimensionality of the wake has resulted in these cases.

3.2. *Velocity field in and around the bubble*

In order to further understand the large bubble behavior with respect to the flow inside and around these bubbles, a series of planar slices of the three-dimensional flow field through the centroid of the bubble are shown in figure 6–9 for cases G3d, G3dd, and G3ddd. The images show the two-dimensional *relative* velocity vectors ($\mathbf{V}_L - \mathbf{V}_B$) superimposed on gray-scale contours corresponding to the three-dimensional relative velocity magnitude (q_{rel}) for which darker areas indicate higher relative velocity magnitudes. It is important to note that the arrow size of the velocity vectors in each slice are scaled by the maximum vector within that slice. In general, the bubble and fluid velocity in the z-direction is small except in the immediate vicinity of the bubble. The figure set includes velocity vectors at $t = 10$ for the x–y plane followed by $t = 15$ for x–y, x–z, y–z planes. All the figures are a close-up near the bubble surface showing only a portion of the domain. The flow around the bubble of case G3 (not shown) is similar to G3D except that it shows even less deformation (Taeibi-Rahni 1995).

In general, bubbles shown in these figures are at bubble Reynolds numbers of about 20, in which the bubble wake (recirculation region) is relatively small as compared to that seen for the rising

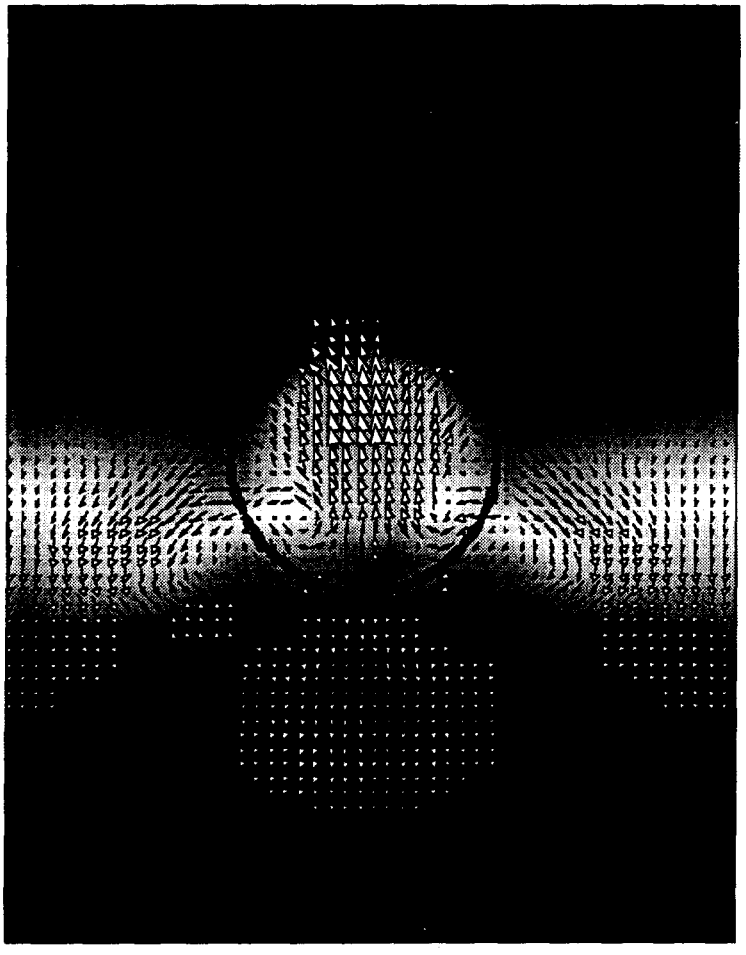

Fig. 9. (a)—(*caption on page* 994)

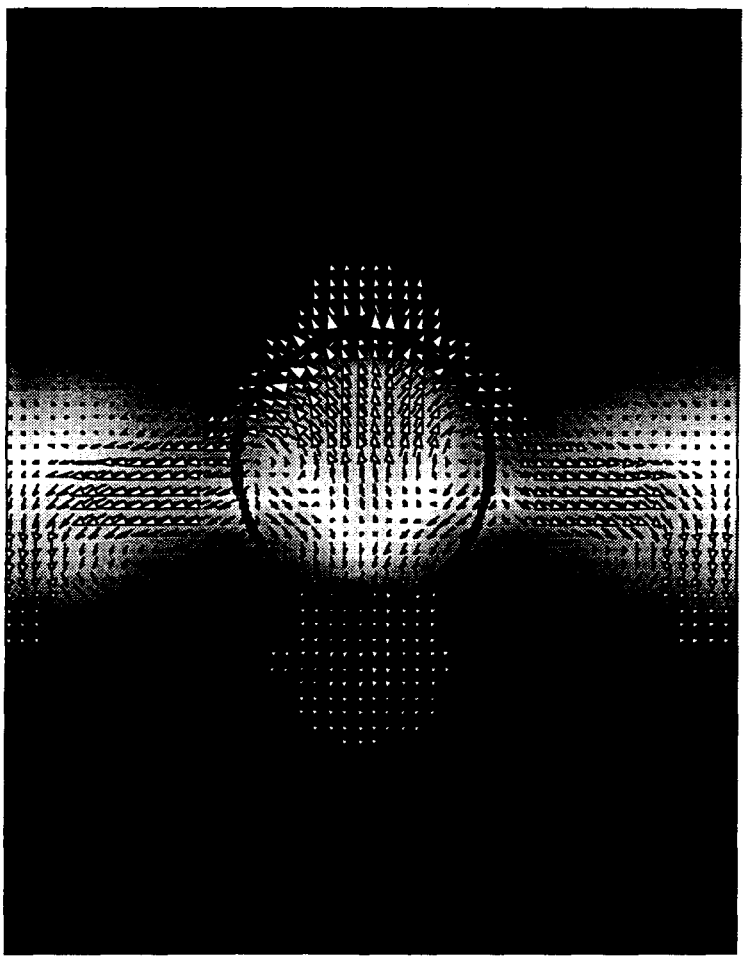

Fig. 9. (b)—(*caption on page* 994)

bubble case (A3) at the same Reynolds number. Previous two-dimensional results (Taeibi-Rahni *et al.* 1996) have also showed the bubble wake to be significantly reduced by being embedded in a shear layer of similar length and time scale as the bubble. It was also noted that there is only a mild symmetric internal recirculation region in the rising bubble flow. Whereas, the free shear layer bubbles (at about the same bubble Reynolds number) can contain strong asymmetric internal recirculation regions as will be demonstrated in the following series of figures.

Figure 6 shows the vector plots for $t = 10$ (5 time units after insertion) for cases G3d, G3dd, and G3ddd. The results indicate a strong recirculation region inside the bubble with one or more core centers, although the location of this point varies. For example, in figure 6(a) this point is close to the lower side of the bubble, since the bottom of the bubble touches the lower ambient liquid, which is moving to the left. The bubble of case G3dd (figure 6(b)) indicates at least two recirculation regions in the x–y plane. On the other hand, the recirculation region has nearly lost all its coherency in case G3ddd (fig. 6(e)), which has a much higher deformation. The ambient liquid recirculation associated by the shear layer left eddy is located on the upper right hand side of the bubble (2 o'clock from center) and to a lesser extent at the lower left hand side (8 o'clock from the center) and it appears to have been elongated as the surface tension decreased. In addition, it clearly influences the internal flow of the bubble for the low surface tension cases, e.g. figure 6(c), for which there is greater movement of the local portions of the bubble surface with respect to the bubble centroid.

At $t = 15$, figure 7 shows exaggerations of the above trends along with additional complications. These are due to the additional deformation as well as the fact that the bubble has dropped further

(c)

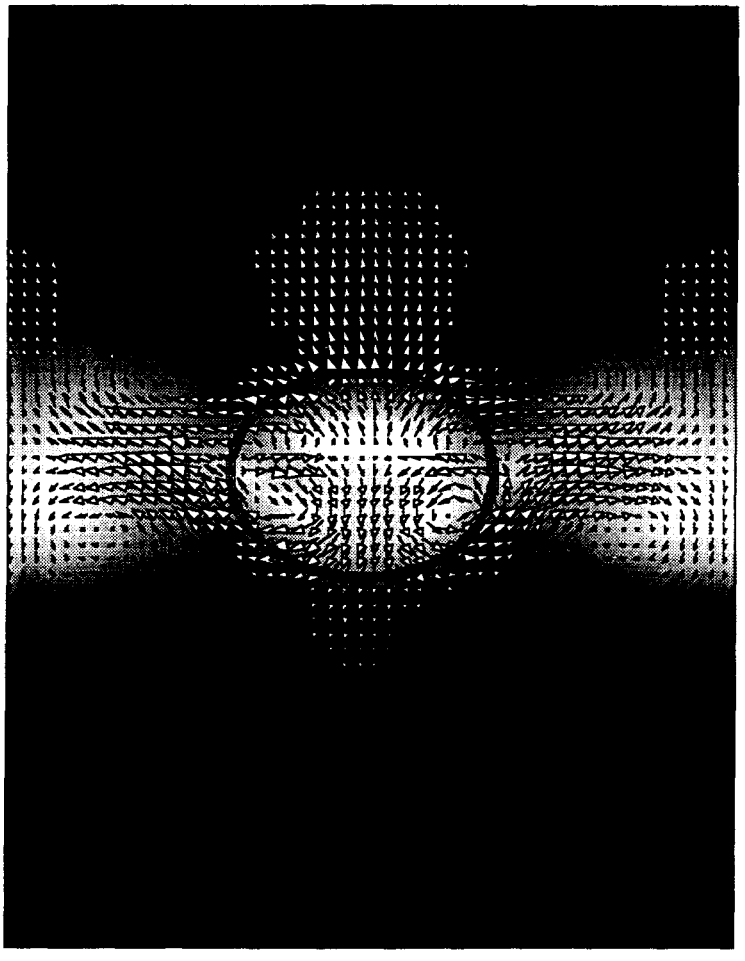

Figure 9. Close-up of relative velocity vectors in the, y–z plane with q_{rel} in the background at $Re_B \sim 11$ corresponding to $t = 15$ for: (a) case G3d ($\sigma = 4$), (b) case G3dd ($\sigma = 1$), (c) case G3ddd ($\sigma = 0.5$).

below the eddy core at later times thus introducing greater asymmetry of the surrounding liquid. The bubbles of case G3d (figure 7(a)) and G3 are both nearly spherical and again show an internal recirculation center at the bottom of the bubble. This is in part due to their descent below the shear layer eddy core. In comparison, the bubbles of cases G3dd and G3ddd (figure 7(b) and (c)) move slower and show greater interaction with the shear layer eddy core. This is a result of the additional resistance of the bubble with respect to the surrounding fluid due to the increased deformability, which yields increased bubble response times. This can be noted explicitly by the reduced bubble Reynolds number as σ reduces (Taeibi-Rahni 1995). In general, the bubble Reynolds numbers continue to increase: they have almost doubled at $t = 20$ with respect to their counterparts at $t = 10$.

Figure 8 display slices of the flow in the x–z plane through the y-centroid of the bubble, where x and z are horizontal and vertical axes, respectively (see figure 1). This plane is essentially parallel to (and at this time within) the shear layer such that velocities vectors in both the $+x$ and $-x$ direction are noted. Thus, the flow far above this plane is uniformly to the right ($+x$ direction) and the flow far below it is uniformly to the left ($-x$ direction). Recall that the external free shear flow is in the x–y plane and is initially set to be invariant in the z-direction. In addition, there was no disturbance added initially in the z-direction and coupled with the low shear layer Reynolds numbers of this study, the spanwise variations for case C3 were negligible. As such, the presence of the three-dimensional patterns seen in the following figures are due solely to the presence of the bubble induced motion in the z direction. Therefore, the leftward jet to the right of the bubble in figure 8(a) can be attributed only to the presence of the bubble.

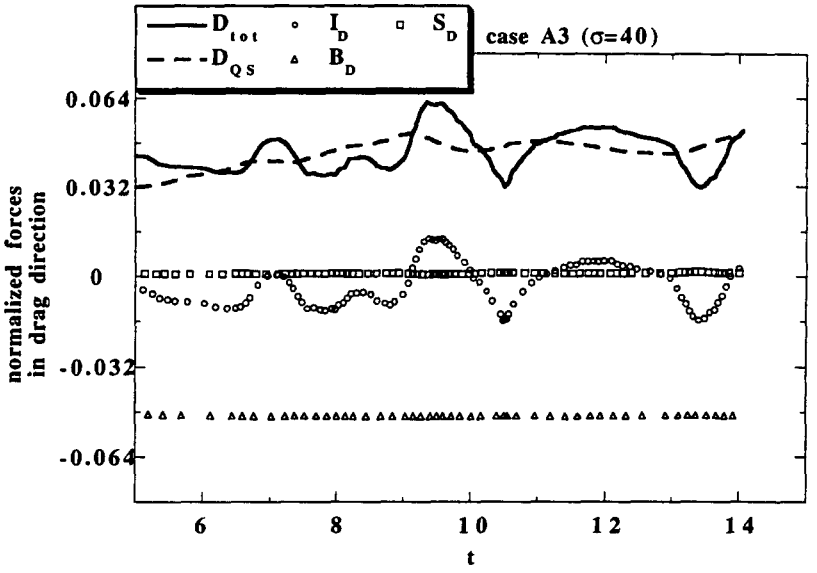

Figure 10. Evolution of different forces on the bubble of case A3 in drag direction using solid sphere drag coefficient and the Sherman (1990) correction for slip conditions at the bubble surface. Uncertainty of predicted forces is approximately 25%.

We are unaware of previous studies which have documented such a jet. The genesis of this relative jet flow may be attributed to the three-dimensional wake of the bubble (to be explained further using y–z plane figures) which tends to increase in strength as surface tension decreases. To understand the jet appearance we should consider that this point would yield a wake in the absolute (vs relative) velocity vector distribution. Once the relative velocity jet flow is generated in x–z plane, it spills around the bubble and causes recirculating regions on the top and bottom of the bubble towards the left hand side. The jet flow is much stronger for case G3dd ($\sigma = 1$) as shown in figure 8(b), where the recirculation regions have moved further above and below the bubble in this figure. Note, deformation is small in this plane but is significant in the x–y plane (figure 7(b)). In case G3ddd (figure 7(c)), strong deformation can be noted and the relative velocity vectors show an additional rightward jet to the left of the bubble constructing two additional vortices on the right hand side of the bubble.

The flow fields near the bubble in the y–z plane are shown for cases G3d, G3dd, and G3ddd in figure 9 for $t = 15$. The two trailing vortices of the three-dimensional bubble wake are apparent in the y–z plane of figure 9(a) (case G3d). These two vortices are more coherent in planes which are downstream (to the right) of the bubble especially for case G3 (Taeibi-Rahni 1995), and yield a significant relative *upwash* at about one-half diameter downstream. This upwash is important as it causes the left ($-x$) running fluid stream below the bubble to be pushed upward and to hit the bubble. This is seen in figure 7(a) where we note the fluid moving toward the left on the lower right-hand side of the bubble—consistent with the jet of figure 8(a). Case G3dd (figure 9(b)) behaves similarly but it's upwash is more exaggerated. Case G3ddd ($\sigma = 0.5$) exhibits a significant degree of deformation even in this plane, which combined with the three-dimensional wake appears to have resulted in four recirculation regions in the y–z plane yielding a downwash and a stronger upwash (figure 9(c)). Some of this upwash can be related to the aerodynamic shape exhibited in figure 7(c).

3.3. *Bubble hydrodynamic forces*

In order to study the bubble dynamics for the different cases, various forces acting on the bubble in the drag and lift directions were investigated during their temporal evolution. As discussed earlier, our bubble dynamics investigation was based on an *a posteriori* analysis of the RBS studies. In other words, once the RBS results (flow fields and bubble trajectories) were obtained, [6] was used to compute the resulting time-evolving drag and lift forces on the bubbles which could then be compared to their quasi-steady values computed by [11], [12].

In the rising bubble case (A3), the total drag grew monotonically until the bubble reached its terminal velocity, at which point the drag approached a roughly constant value equal to the buoyancy force (figure 10). We note some oscillations are observed, which are consistent for the values of Morton and Bond number selected (table 1), which are known to yield a wobbly bubble rise (Clift *et al.* 1978). The quasi-steady drag time history was also computed (from [11]) and shown on this figure. As expected, it was quite similar to the total drag time history both qualitatively and quantitatively. Mei's (1994) quasi-steady drag coefficient was also investigated for comparison, however it significantly underpredicted (by about 20%) the total drag.

The evolution of forces in the drag direction for case G3 ($\sigma = 40$) is shown in figure 11(a). From this figure, buoyancy and drag are the dominant forces (although we must keep in mind that the uncertainty of these forces is roughly 25%). The bubble in this case typically moves in the gravity direction (opposing buoyancy) and therefore the component of the buoyancy force in the drag direction is maximized. We note that the small $\mathbf{V}_{rel}$ of this case yields a small $\mathbf{D}_{QS}$ about which $\mathbf{D}_{tot}$ has strong oscillations, which corresponds to large adjunct drag forces ($\mathbf{D}_{tot} - \mathbf{D}_{QS}$) similar to cylindrical bubble results (Taeibi-Rahni *et al.* 1996). The evolution of forces in the lift direction for case G3 ($\sigma = 40$) is shown in figure 11(b). From this figure, note that the total lift also fluctuates about the quasi-steady lift yielding an adjunct lift force ($\mathbf{L}_{tot} - \mathbf{L}_{QS}$) which is on the average roughly

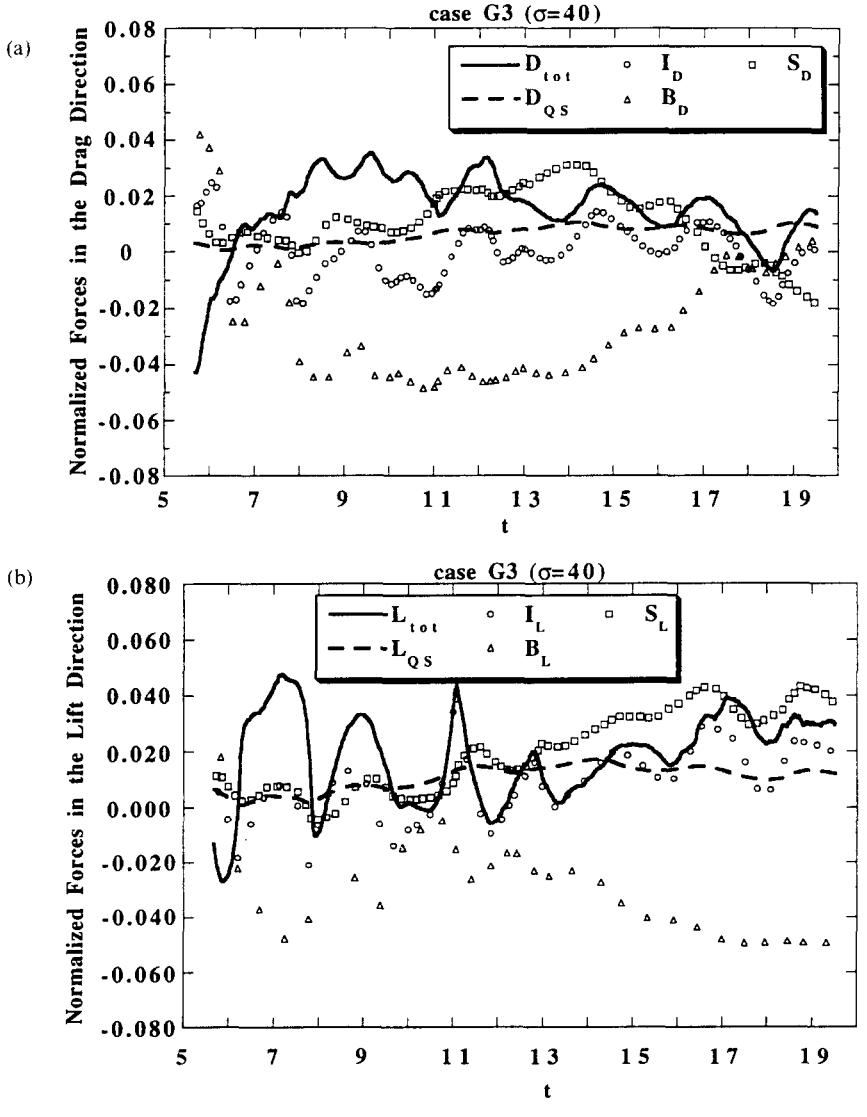

Figure 11. Evolution of forces for case G3 in (a) the drag direction and (b) the lift direction.

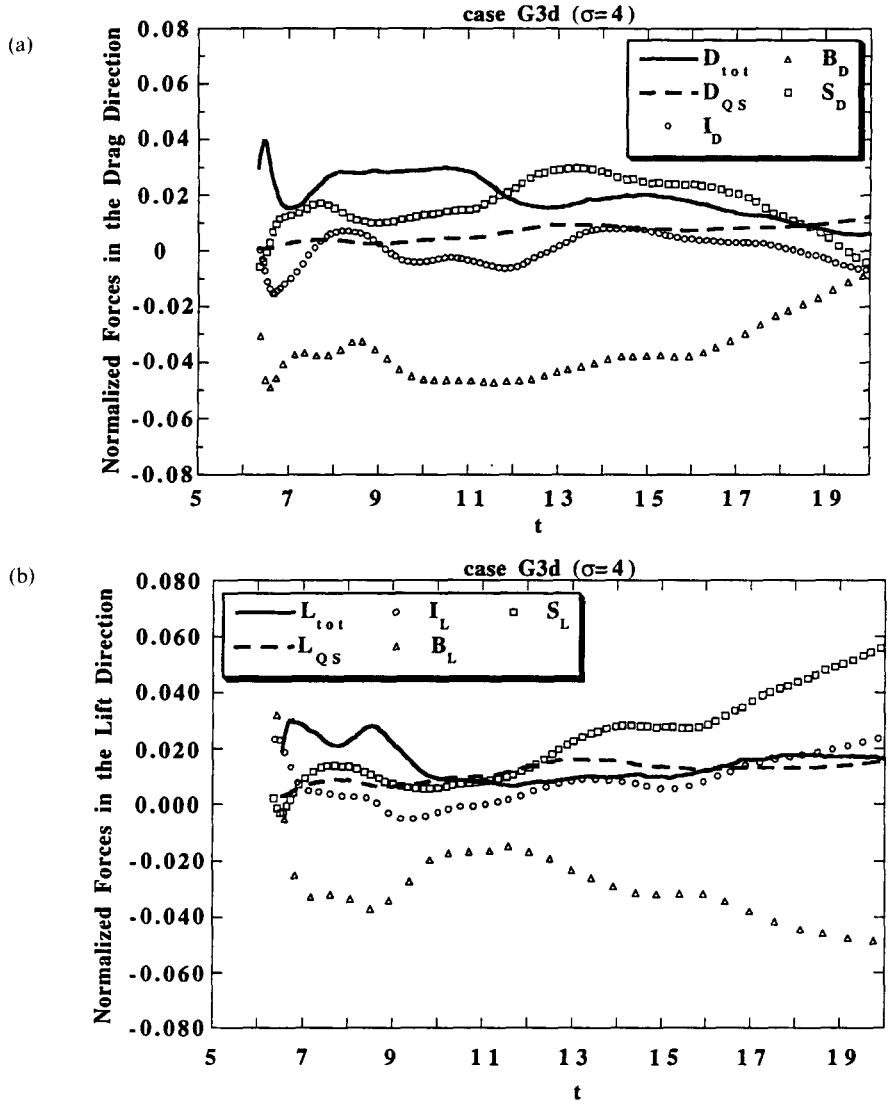

Figure 12. Evolution of forces for case G3d in (a) the drag direction and (b) the lift direction.

zero. The timescale of these fluctuations (~ 2) roughly correspond to a bubble response time estimated from the average relative velocity (Taeibi-Rahni 1995). The results indicates that the quasi-steady lift coefficient of 0.5 (Auton *et al.* 1988) may be reasonable only in a time-averaged sense. In addition, note the significance of stress gradient at the later times as the bubble moves out of the eddy core and the bubble relative velocity increases and is subjected to higher shear.

The hydrodynamic forces were also calculated for the relaxed deformation cases G3d (figure 12), G3dd, and G3ddd. In general, the total drag is significantly greater than quasi-steady drag, e.g. figure 12(a). This underprediction of the quasi-steady drag force was even greater as surface tension decreased for cases G3dd and G3ddd (Taeibi-Rahni 1995). This is attributed to the higher drag coefficients for deformable bubbles (Soo 1989), which are not accounted for by the current (spherical) quasi-steady drag coefficient. In addition, there is a significant increase in the adjunct force oscillation time scale in the relaxed deformation bubbles (cases G3dd and G3ddd). This can also be attributed to the higher drag coefficients which yield larger bubble response times.

The lift force is reasonably represented on a time-averaged basis for case G3d as was found for case G3. Again there are also significant adjunct lift forces, albeit at a longer timescale of fluctuation as compared to case G3. A similar result is seen for case G3dd but case G3ddd actually shows total lift forces which were in general *opposite* in sign as the quasi-steady lift forces. This is consistent with experiments by Kariyasaki (1987) and simulations by Ervin (1993).

The issue of proportionality of lift to vorticity [$a_B\omega$ vs $(v\omega)^{1.2}$] mentioned in section 2.2 is investigated using the bubble lift forces. The RBS total lift force for each case was converted to both an inviscid type lift coefficient (C_L using [12]) and a viscous lift coefficient (C_{Lv} using [13]). These were then compared to their two respective quasi-steady values (C_{LQS} and C_{LvQS}). Figure 13 shows that both lift coefficients are reasonably represented on average by their quasi-steady values for cases G3 and G3d, and perhaps the C_L values exhibit a somewhat better agreement than the C_{Lv} values (where the Sridhar and Katz suggested value of C_{LvQS} of 12.18 was used). Unfortunately, the small data set and the small variation in vorticity do not allow a general conclusion. Notably, as the surface tension decreases neither C_{LQS} or C_{LvQS} were reasonable approximations, e.g. case G3ddd yielded total lift coefficients of opposite sign to both quasi-steady counterparts.

3.4. Resolved bubble vs point bubble trajectories

Finally, in order to compare large bubble and point bubble convection, trajectories of point bubbles (for different quasi-steady approximations) were calculated using the method described in section 2.3. As such, [6] but with quasi-steady drag and lift forces was employed to calculate point bubble accelerations, velocities and trajectories. These could then be compared to the RBS trajectories which involved no 'modeling' of the drag and lift forces. This portion of the study was intended to evaluate the significance of lift and drag formulations on bubble advection for the present non-linear flow field.

The trajectories and velocities of the large bubbles of cases G3, G3d, G3dd, and G3ddd in the x–y, y–z and x–z planes are discussed in Taeibi-Rahni (1995). From these results, the bubble motion in the z-direction is negligible except for some mild bubble wobble for the high deformation cases. Therefore, we will only show x–y trajectories herein. Figure 14 gives point bubble trajectories using several different C_D and C_L formulations and the RBS trajectory for case G3, which would be expected to be best represented by the quasi-steady expressions since it has the least deformation. One point bubble formulation employs C_D equal to infinity, which simply corresponds to following the liquid velocity exactly. Comparison of the different trajectories leads to the following conclusions: (a) the combination of the Auton *et al.* (1988) lift coefficient and the drag coefficient adjusted as per Sherman (1990) provides the most reasonable point bubble trajectory; (b) when C_L is small compared to C_D (e.g. $C_L = 0$, $C_L = C_{LMei}$ or C_D equal to infinity), the point bubble curls upward and begins to convect to the right; and (c) the large (RBS) bubble trajectory is not well

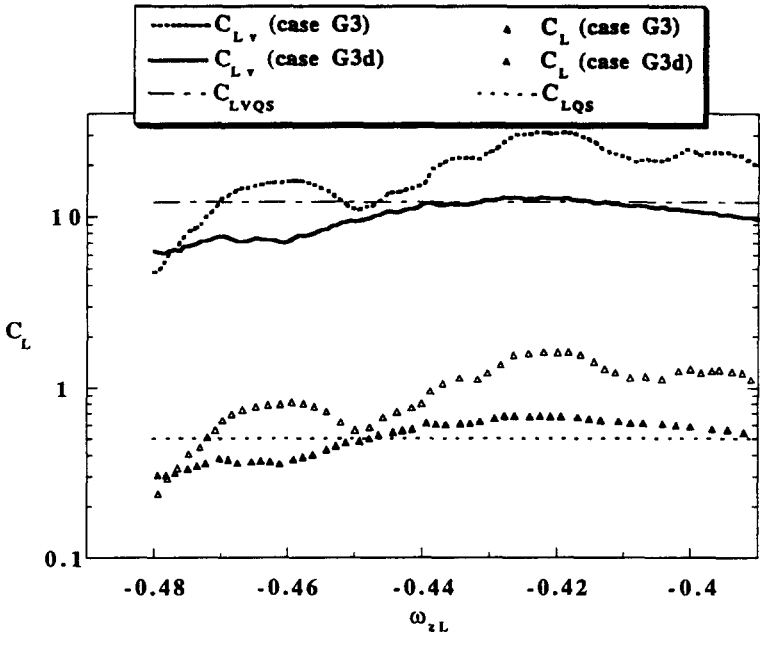

Figure 13. Bubble lift coefficient vs the average liquid vorticity around the bubble using two different definitions for C_L. Uncertainty of predicted values is approximately 35%.

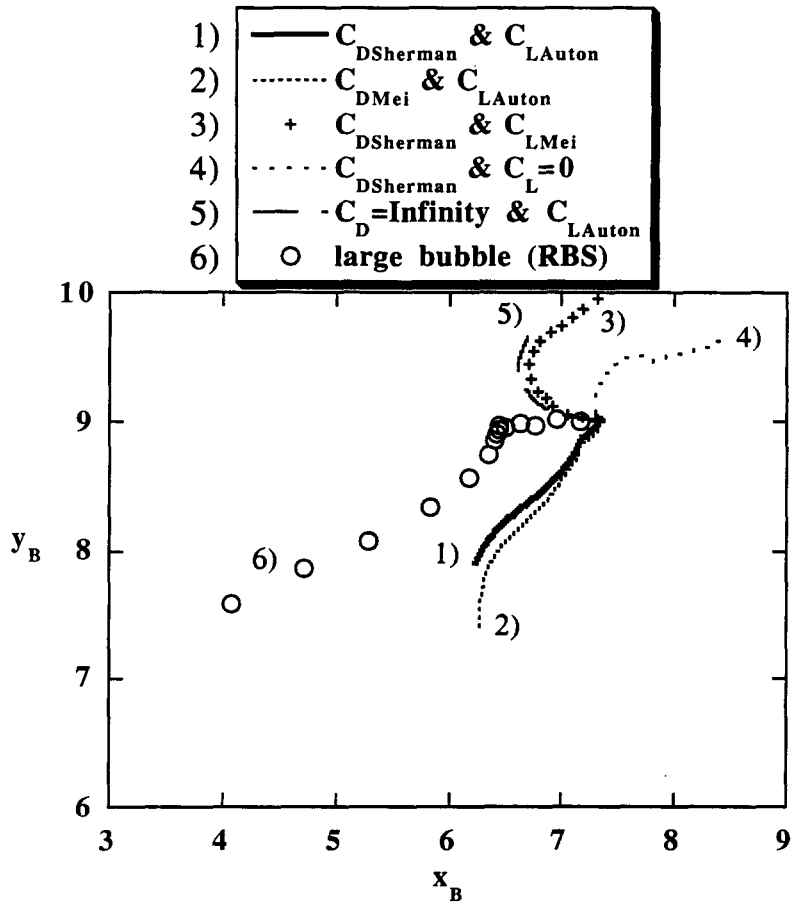

Figure 14. Trajectories for the large RBS bubble of case G3 and for spherical point bubbles using various drag coefficients: that of White (1991) as adjusted by Sherman (1990), that of Mei (1994a), and a drag coefficient of infinity; and various lift coefficients: Auton *et al.* (1988), Mei (1994b) lift coefficient, and a zero lift coefficient.

predicted by any of the point bubble cases studied. The strong variations among the point bubble trajectories with different quasi-steady drag and lift expressions are in part caused by the non-linear flow field and the sensitivite initial placement of the bubble in the eddy core.

4. CONCLUSIONS

The present study investigated a few cases of large deformable bubbles embedded in a non-linear free shear layer. The test conditions were chosen such that bubble length and time scales were similar to that of the free shear layer, thus introducing the potential for strong interaction. Examining the three-dimensional velocity vector distributions, the bubbles were found to produce complex wakes due to interaction with the shear layer. This resulted in to novel jets and recirculation regions within and around the bubble, especially at low surface tension values.

By solving the detailed flow around and inside the bubble, the RBS hydrodynamic forces and trajectories could also be compared with those expected from quasi-steady classical predictions. Computation of RBS forces on the bubble generally indicated that for the large bubble with negligible deformation (nearly spherical), on *average* the drag roughly follows the 2/3 correction for particles with slip surfaces and on *average* the lift roughly follows the potential flow results. However, significant temporal fluctuations about these corresponding quasi-steady values were seen for both lift and drag. As deformation increased, the quasi-steady drag began to underpredict the actual drag and the quasi-steady lift predicted values of *opposite* sign to that of the actual lift for very high deformation. As with the low deformation case, significant temporal excursions from

these quasi-steady values were noted (caused by the non-linear spatial and temporal gradients of the surrounding liquid). In general, the hydrodynamic forces on the low-deformation bubbles showed much higher frequencies of these excursions than the high deformation cases, which followed the liquid flow with much more resistance.

Finally, bubble trajectories based on a point bubble approximation were much different than that based on the large bubble RBS calculation, presumably due to the above temporal fluctuations of the bubble total lift and drag forces. However, large differences were noted even among the different point bubble trajectories which were based on a variety of quasi-steady expressions for lift and drag for the point bubble dispersion; this is in part due to the non-linear flow field and the sensitivite initial placement of the bubble in the eddy core.

Acknowledgements—This work was supported by the Office of Naval Research (ONR) under contract N00014-95-1-0313 with Dr Edwin Rood as technical monitor. The Pittsburgh Supercomputing Center under grant number CTS940048P furnished the Cray computer time used for the numerical calculations.

REFERENCES

Auton, T. R., Hunt, J. C. R. and Prud'Homme, M. (1988) The force exerted on a body in inviscid unsteady non-uniform rotational flow. *J. Fluid Mech.* **197,** 241–257.

Chahine, G. L., Delepoule, E. and Hauwaert, P. (1993) Study of the interaction between a bubble and a vortical structure. In *ASME, Cavitation and Multiphase Flow Forum*, FED Vol. 153, pp. 39–46.

Chahine, G. L. and Duraiswami, R. (1992) Dynamical interactions in a multi-bubble cloud. *J. Fluids Eng.* **114,** 680–686.

Clift, R., Grace, J. R. and Weber, M. E. (1978) *Bubbles, Drops, and Particles*. Academic Press, New York.

Ervin, E. A. (1993) Computations of bubbles and drops in shear flow. Ph.D. dissertation, Department of Mechanical Engineering, University of Michigan, Ann Arbor, MI.

Jiang, R. L., Varty, R. L. and Sigurdson L. W. (1993) The acceleration of a single bubble rising from a nozzle in water. In *ASME, Gas–Liquid Flows*, FED Vol. 165, pp. 161–169.

Kojima, E., Akehata, T. and Shirai, T. (1975) Behavior of single air bubbles held stationary in downward flows. *J. Chem. Eng. Japan* **8,** 108–113.

Kariyasaki, A. (1987) Behavior of a single gas bubble in a liquid flow with a linear velocity profile. In *Proc. of the* 1987 *ASME–JSME Thermal Engineering Joint Conference*, pp. 261–267. ASME, New York.

Kuo, J. T. and Wallis, G. B. (1988) Flow of bubbles through nozzles. *Int. J. Multiphase Flow* **14,** 547–564.

Loth, E. and Cebrzynski, M. S. (1995) Modulation of shear layer thickness due to large bubbles. *Int. J. Multiphase Flow* **21,** 919–927.

Lovalenti, P. M. and Brady, J. F. (1993) The force on a bubble, drop, or particle in arbitrary time-dependent motion at small Reynolds number. *Physics of Fluids A* **5,** 2104–2116.

Maxey, M. R. and Riley, J. J. (1983) Equation of motion for a small rigid sphere in a non-uniform flow. *Phys. Fluids* **26,** 883–889.

Mei, R., Lawrence, C. J. and Adrian, R. J. (1991) Unsteady drag on a sphere at finite Reynolds number with small fluctuations in the free-stream velocity. *J. Fluid Mech.* **233,** 613–631.

Mei, R., Klausner, J. F. and Lawrence, C. J. (1994) A note on the history force on a spherical bubble at finite Reynolds number. *Phys. Fluid* **6,** 418–420.

Metcalfe, R. W., Orszag S. A., Brachet, M. E., Menon, S. and Riley, J. J. (1987) Secondary instability of a temporally growing mixing layer. *J. Fluid Mech.* **184,** 207–243.

Oakley, T., Loth, E. and Adrian, R. J. (1995) A study of bubble dispersion in turbulent free shear layer using cinematic PIV. *ASME/JSME Fluids Engineering Conference*, Hilton Head, SC, August.

Odar, F. and Hamilton, W. (1964) Forces on a sphere accelerating in a viscous fluid. *J. Fluid Mech.* **18,** 302–314.

Peskin, C. S. (1977) Numerical analysis of blood flow in the heart. *J. Comp. Phys.* **25,** 220–252.

Saffman, P. G. (1956) On the rise of small air bubbles in water. *J. Fluid Mech.* **1,** 249–275.
Sangani, A. S. and Didwania, A. K. (1993) Dynamic simulations of flows of bubbly liquid at large Reynolds numbers. *J. Fluid Mech.* **250,** 307–337.
Sherman, F. S. (1990) *Viscous Flow*. McGraw-Hill, New York.
Soo, S. L. (1976) Net effect of pressure gradient on a sphere. *Phys. Fluids* **19,** 757–757.
Sridhar, G. and Katz, J. (1993) Lift and drag forces on bubbles entrained by a vortex ring. In *ASME, Cavitation and Multiphase Flow Forum*, FED Vol. 153, pp. 165–170.
Taeibi-Rahni, M. and Loth, E. (1996) Forces on a large cylindrical bubble in an unsteady rotational flow. *Amer. Inst. of Chem. Eng. J.* **42,** 638–648.
Taeibi-Rahni, M., Loth. E. and Tryggvason, G. (1994) Flow modulation of a planar free shear layer with large bubbles—direct numerical simulations. *Int. J. Multiphase Flow* **20,** 1109–1128.
Taeibi-Rahni, M. (1995) Direct numerical simulation of large bubbles in a free shear layer. Ph.D. dissertation, Department of Aeronautical and Astronautical Engineering, University of Illinois at Urbana—Champaign, Urbana, IL.
Unverdi, S. and Tryggvason, G. (1992a) A front-tracking method for viscous, incompressible, multi-fluid flows. *J. Comp. Phys.* **100,** 25–37.
Unverdi, S. and Tryggvason, G. (1992b) Computations of multi-fluid flows. *Physica D* **60,** 70–83.
White, F. M. (1991) *Viscous Fluid Flow*, 2nd edition. McGraw-Hill, New York.
Yang, Y. and Leal, L. G. (1991) A note on memory-integral contributions to the force on an accelerating spherical drop at low Reynolds number. *Phys. Fluids A* **3,** 1822–1824.